

# A Predictive Approach To Enhance Time-Series Forecasting

Skye Gunasekaran<sup>1</sup>, Assel Kembay<sup>1</sup>, Hugo Ladret<sup>2</sup>, Rui-Jie Zhu<sup>1</sup>, Laurent Perrinet<sup>3</sup>, Omid Kavehei<sup>4</sup>, Jason Eshraghian<sup>1\*</sup>

<sup>1</sup>Department of Electrical and Computer Engineering, University of California, Santa Cruz, CA, USA

<sup>2</sup>Friedrich Miescher Institute for Biomedical Research, Basel, Switzerland

<sup>3</sup>Institut de Neurosciences de la Timone, Aix Marseille Univ, CNRS, Marseille, France

<sup>4</sup>School of Biomedical Engineering, The University of Sydney, Sydney, Australia

\* Corresponding author: jsn@ucsc.edu

## Abstract

Accurate time-series forecasting is crucial in various scientific and industrial domains, yet deep learning models often struggle to capture long-term dependencies and adapt to data distribution shifts over time. We introduce Future-Guided Learning, an approach that enhances time-series event forecasting through a dynamic feedback mechanism inspired by predictive coding. Our method involves two models: a detection model that analyzes future data to identify critical events and a forecasting model that predicts these events based on current data. When discrepancies occur between the forecasting and detection models, a more significant update is applied to the forecasting model, effectively minimizing surprise, allowing the forecasting model to dynamically adjust its parameters. We validate our approach on a variety of tasks, demonstrating a 44.8% increase in AUC-ROC for seizure prediction using EEG data, and a 23.4% reduction in MSE for forecasting in nonlinear dynamical systems (outlier excluded). By incorporating a predictive feedback mechanism, Future-Guided Learning advances how deep learning is applied to time-series forecasting.

**Keywords:** Time Series, Event Prediction, Predictive Coding, Deep Learning

## Introduction

In recent years, deep learning models have been increasingly applied to time-series forecasting, leveraging their ability to model complex, nonlinear relationships within data [1]. Despite these advancements, challenges remain in accurately capturing long-term dependencies due to inherent stochasticity and noise in signals. Time-series data involve complex temporal dynamics and often exhibit non-stationary behaviors. Additionally, they are frequently subject to external influences and perturbations which introduce abrupt changes in the data patterns, making long-term forecasting difficult. As a result, even advanced deep learning models face difficulties when tasked with long-term predictions [2, 3].

Complementary to these deep learning approaches, classical time-series methods have long used threshold-based adaptation to capture sudden distributional shifts. Early methods such as the Page–Hinkley test and the Drift Detection Method (DDM) formalize this by keeping a running estimate of error statistics, and raising an alarm when a significant change in data distribution is observed [4, 5]. Once drift is detected, models are either fine-tuned on recent labeled examples or retrained from scratch on a sliding window of past data. This threshold-retraining approach has shown practical performance in domains ranging from anomaly detection to predictive maintenance [6], but it can suffer from abrupt resets, loss of long-term knowledge, and sensitivity to hyperparameter choices for the error threshold.

Beyond these classical methods, several self-supervised approaches use future prediction as a pretext task: given an input  $x_t$ , they learn to reconstruct  $x_{t+n}$ . This includes applications from video frame prediction [7] to masked audio modeling [8]. However, because they decouple pretraining from online correction, they do not incorporate continuous feedback from each new observation. As a result, their forecast errors cannot be dynamically adjusted as more data arrives.

To address these challenges, we introduce Future-Guided Learning (FGL), an approach that draws on predictive coding and employs a dynamic feedback mechanism to enhance time-series event forecasting. By leveraging a future-oriented forecasting model that guides a past-oriented forecasting model, FGL introduces a temporal interplay reminiscent of Knowledge Distillation (KD) [9], where a “teacher” can provide insights that improve a “student” model’s long-horizon predictions.

Other works have explored the application of knowledge distillation to sequential data, such as speech recognition [10–12] and language modeling [13], and have excelled at transfer learning and model compression. While these show value in the application of KD to sequential data, it is not used to *enhance* performance over the baseline. KD can be used to enhance how a model handles temporal dynamics and variance in uncertainty across a time-horizon.

Importantly, FGL is rooted in the theory of predictive coding, a theory which treats the brain as a temporal inference engine that refines its internal model by minimizing “prediction errors” [14–17]—the discrepancy between expected and actual inputs—over time and across hierarchical layers of abstraction, progressively building internal models of the world [18, 19].

Although predictive coding naturally handles spatio-temporal data, it has yet to penetrate mainstream deep learning [20, 21]. Neural Predictive Coding frameworks

aim to fill this gap by coupling prediction and error-correction in a unified loop. For example, Oord et al. [22] use an autoencoder to forecast future latent representations, and Lotter et al.’s PredNet [23] stacks LSTM cells that propagate and correct layer-wise prediction errors. While these frameworks offer valuable neuroscientific insights, they often emphasize biological plausibility over empirical forecasting performance and tend to be restricted to specific architectures or domains. As a result, it remains challenging to apply them to diverse time-series tasks, thus motivating the need for a more flexible and performance-driven framework, such as FGL.

We evaluate FGL in two settings (see Supplementary Note 4): (1) EEG-based seizure prediction, where FGL boosts AUC-ROC by 44.8% on average across patients; and (2) Mackey–Glass forecasting, achieving a 23.4% MSE reduction. These results show that FGL not only enhances accuracy but also offers a principled way to leverage uncertainty over time, directly aligning with predictive-coding theory.

## Results

We briefly summarize the two domains in which FGL is evaluated:

- *Event prediction*, where a pretrained seizure-detection “teacher” model distills near-future information into a “student” model tasked with early event prediction. We benchmark on two standard EEG datasets (CHBMIT and AES) and report area-under-ROC improvements relative to strong baselines (MViT and CNN-LSTM).
- *Regression forecasting*, in which we reformulate continuous signal forecasting as a categorical task by *discretizing* each true value  $x_{t+n}$  into one of  $B$  equal-width intervals (or “bins”). The student predicts a distribution over these  $B$  bins via softmax—matched to the teacher’s softened logits via KL-divergence—while the hard one-hot bin label remains in the cross-entropy term. Final predictions are recovered as the expectation over bin centers, and performance is measured by the resulting mean squared error (MSE). We explore two resolutions ( $B = 25$  vs.  $B = 50$ ) to show how bin granularity trades off difficulty against tighter uncertainty bounds.

### Event Prediction Results

To compare our method with state-of-the-art (SOTA) approaches, we tested FGL against a Multi-Channel Vision Transformer (MViT) [24] and a CNN-LSTM [25, 26]. These models are commonly used in medical settings for temporal data and have demonstrated strong efficacy. Further details, including results on false positive rate (FPR) and sensitivity, are provided in Supplementary Note 1.

On the CHBMIT dataset, our results show a significant improvement with FGL compared to the baseline, with an average 44.8% increase in the area under the receiver operating characteristic curve (AUC-ROC), as shown in Fig. 2(a-c). Additionally, FGL enhanced predictions across most patients, with the largest gain observed for patient 5 by a factor of  $3.84\times$ . The performance dropped only for patient 23 by a factor of  $0.80\times$  compared to the CNN-LSTM, but still significantly outperformed the MViT architecture.

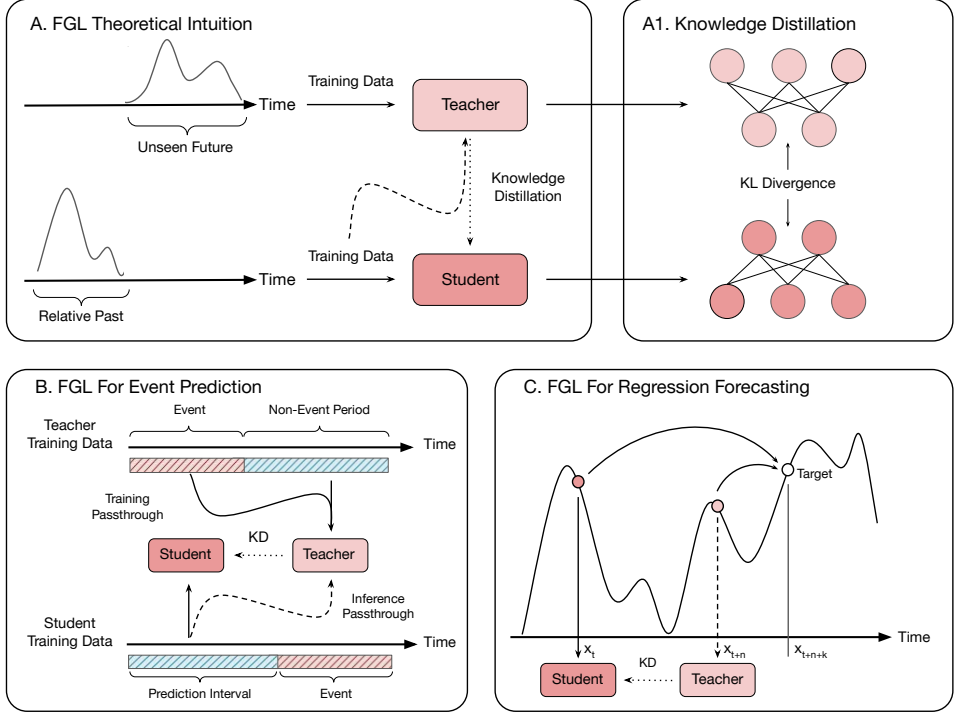


**Fig. 1: Overview of FGL and its applications** (A) In the FGL framework, a teacher model operates in the relative future of a student model that focuses on long-term forecasting. After training the teacher on its future-oriented task, both models perform inference during the student’s training phase. The probability distributions from the teacher and student are extracted, and a loss is computed based on Equation 1. (A1) Knowledge distillation transfers information via the Kullback-Leibler (KL) divergence between class distributions. (B) In an event prediction setting, the teacher is trained directly on the events themselves, while the student is trained to forecast these events. Future labels are distilled from the teacher to the student, guiding the student to align more closely with the teacher model’s predictions, despite using data from the relative past. (C) In a regression forecasting scenario, the teacher and student perform short-term and long-term forecasting, respectively. Similar to event prediction, the student gains insights from the teacher during training, enhancing its ability to predict further into the future.

On the AES dataset, where the teacher model was trained on a different set of seizure patients and then used on new individuals at test time, FGL still achieved an average performance improvement of 8.9% over the CNN-LSTM, as shown in Fig. 2(b). Further details on implementation and preprocessing are provided in Supplementary Note 1.

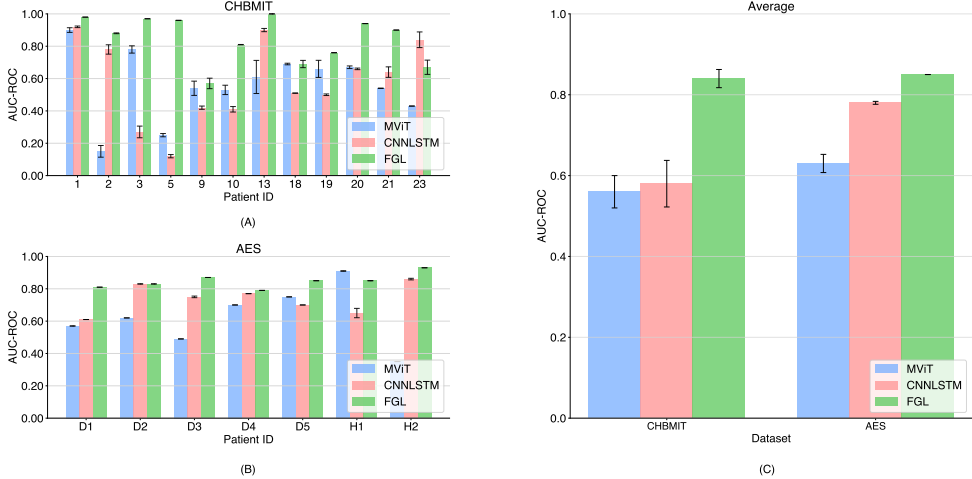


**Fig. 2: Seizure Prediction results on (a) CHBMIT, (b) AES and (c) dataset averages .** Three methods are tested: an MViT, a CNN-LSTM, and FGL. All results were calculated over 3 continuous trials. The means and variance bars are reported.

## Regression Forecasting Results

Across both bin resolutions, incorporating future-guided learning (FGL) yields substantial average MSE reductions versus the baseline. With 25 bins, the baseline's average error is 4.09, while the students trained with FGL achieve 3.64 ( $\alpha = 0.0$ ) and 3.56 ( $\alpha = 0.5$ )—a 11–13% improvement. When the task is made harder (50 bins), the baseline error jumps to 28.34, but FGL cuts that by more than half to 11.95( $\alpha = 0.0$ ) and 11.68 ( $\alpha = 0.5$ ). The consistent edge of the ( $\alpha = 0.5$ ) student over its ( $\alpha = 0.0$ ) counterpart (even if modest) confirms that blending distilled future information with ground-truth targets during training provides a measurable boost.

## Discussion

Overall, our experiments demonstrate that FGL consistently enhances both event-prediction and regression-forecasting tasks by leveraging near-future information to guide long-horizon student models. Below, we examine the distinct gains and underlying mechanisms in each domain, and highlight key trade-offs and robustness benefits.

### Event Prediction

On both the CHBMIT and AES datasets, FGL yields substantial increases in AUC-ROC and noticeably tighter error bars compared to our CNN-LSTM and MViT baselines (Fig. 2c). This variance reduction is particularly important in seizure forecasting, where few seizure events per patient can otherwise lead to unstable performance.

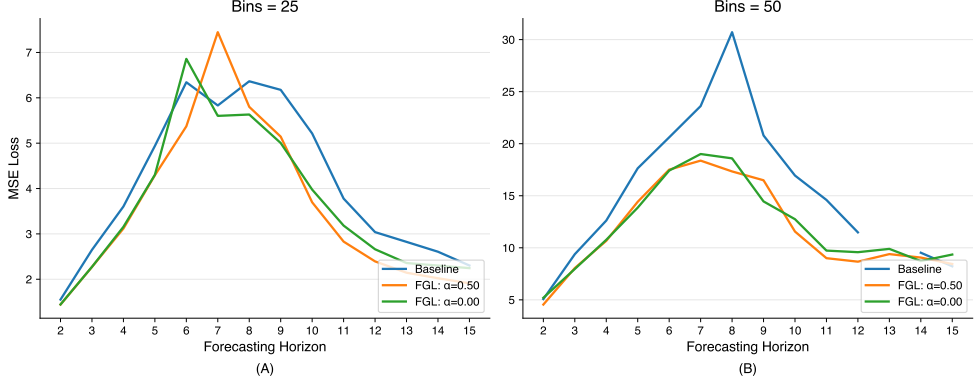


**Fig. 3: Mackey–Glass forecasting results with (A) 25 and (B) 50 bins.** Results show the MSE loss at each horizon. In panel (B), the baseline MSE at horizon 13 was a large outlier and has been omitted for clarity. (A & B)  $\alpha = 0.00$  indicates the student trained using only the distilled label, and  $\alpha = 50$  indicates a balance of distilled and ground-truth labels. A table of results is available in Supplementary Note 2.

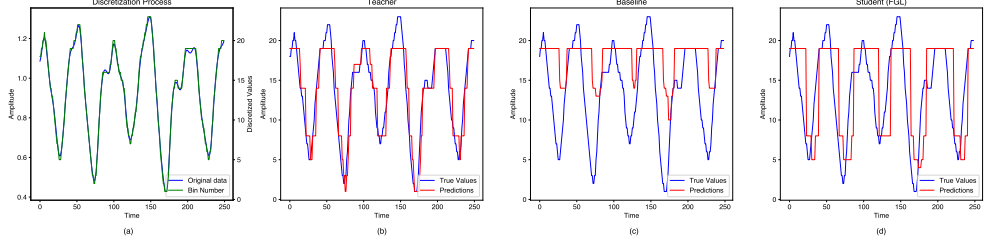


**Fig. 4: Discretization enables knowledge-distillation on Mackey–Glass.** (a) After generating the chaotic trajectory, every scalar target  $X_{t+\ell}$  is *quantized* into one of  $C$  equal-width bins. The regression problem is thus recast as  $C$ -way classification, so the teacher and student can exchange *soft logits* of identical dimensionality—an essential requirement for the KL-distillation term in FGL. (b) Teacher performs next-step prediction. (c) Baseline performs a 5-step forecast without future guidance. (d) FGL-trained student forecasting the same horizon. By aligning its logit distribution with the teacher’s near-future logits, the FGL student captures neighborhood information in bin space, yielding a visibly lower MSE and a smoother reconstruction.

A critical factor is the choice of teacher model. With CHBMIT, we trained patient-specific teachers, which captured individual epileptic signatures and delivered the largest average boost (44.8% AUC-ROC) but also higher inter-patient variability. By contrast, our “universal” teachers for AES—pretrained on aggregated UPenn–Mayo seizure data—achieved more modest gains (8.9%) yet produced consistent improvements across all test subjects. Thus, there is a clear trade-off between tailoring

guidance to each patient versus exploiting larger, heterogeneous training sets. In practice, one might combine both approaches: use a universal teacher to establish a stable baseline and then fine-tune patient-specific models where data allow.

## Regression Forecasting

In the Mackey–Glass experiments, FGL again outperforms the baseline by a wide margin, cutting MSE by 11–13% at 25 bins and by over 50% at 50 bins (Fig. 3). Here, the teacher’s short-horizon forecasts serve as a dynamic “upper bound” that guides the student away from catastrophic errors. Rather than penalizing the student harshly whenever the teacher itself errs, our KL-based distillation captures the teacher’s uncertainty patterns, yielding a smoother, more informative loss surface.

Examining individual horizons reveals that FGL not only lowers overall error but also produces a gentler, more predictable degradation as the forecast horizon increases. At 25 bins, baseline MSE rises from 1.55 at horizon 2 to 2.30 at horizon 15, whereas FGL students exhibit a flatter slope and smaller peaks. When using 50 bins—where the baseline suffers extreme outliers (e.g., MSE = 195.62 at horizon 13)—both FGL variants cap errors below 12, underscoring dramatic robustness gains in chaotic settings.

## Key Insights and Future Directions

Across both tasks, FGL’s effectiveness hinges on two principles: (1) distilling uncertainty from a more confident, near-future teacher and (2) blending distilled signals with ground-truth targets to stabilize learning. Moving forward, we plan to explore hybrid schemes that adaptively weight patient-specific and universal teachers, as well as extensions to multi-horizon and multi-modal forecasting. Finally, integrating FGL with online drift-adaptation methods (e.g., Page–Hinkley) could further enhance resilience to non-stationary environments without discarding long-term knowledge.

## Methods

Traditional KD involves transferring probabilistic class information between two models that share the same representation space. In our approach, we reformulate this student-teacher dynamic by placing the teacher model in the relative future of the student model, introducing a temporal difference in the representation space between them.

Our distillation method follows that of Hinton et al. [9], where the student model is trained using a combination of the cross-entropy loss with the ground truth labels and the Kullback–Leibler (KL) divergence between the softmax outputs of the student and teacher models. This dual objective allows the student to learn from both the true data and the future-oriented predictions of the teacher.

**Notation:** Let  $x_t \in \mathcal{X}$  be the input observed up to time  $t$ , and  $y_{t+\ell} \in \mathcal{Y}$  the target at horizon  $\ell$ . We denote by

$$T_\phi : \mathcal{X} \rightarrow \mathbb{R}^C \quad \text{and} \quad S_\theta : \mathcal{X} \rightarrow \mathbb{R}^C$$

two neural network models parameterized by  $\phi$  and  $\theta$ , producing  $C$ -dimensional *logits*. The teacher  $T_\phi$  forecasts  $n$  steps ( $y_{t+n}$ ), while the student  $S_\theta$  forecasts  $n+k$  steps ( $y_{t+n+k}$ ).

**Claim 1** (Future-Guided Learning (FGL)). *Let*

$$T_\phi(x_t) \approx y_{t+n}, \quad S_\theta(x_t) \approx y_{t+n+k},$$

*be the logits of a teacher forecasting  $n$  steps ahead and a student forecasting  $n+k$  steps. FGL trains the student by minimizing:*

$$\mathcal{L}_{\text{FGL}}(\theta) = \underbrace{\alpha \mathcal{L}_{\text{task}}(S_\theta(x_t), y_{t+n+k})}_{\text{task loss}} + \underbrace{(1-\alpha) \tau^2 \text{KL}\left(\sigma\left(\frac{T_\phi(x_{t+k})}{\tau}\right) \parallel \sigma\left(\frac{S_\theta(x_t)}{\tau}\right)\right)}_{\text{future-guided distillation}}, \quad (1)$$

*where  $\sigma$  is softmax,  $\tau$  the distillation temperature, and  $0 < \alpha < 1$  balances ground truth and teacher guidance. By aligning the teacher’s  $n$ -step logits at  $t+k$  with the student’s  $(n+k)$ -step logits at  $t$ , FGL transfers near-future uncertainty to the long-horizon forecaster.*

The first term in  $\mathcal{L}_{\text{FGL}}$  ensures the student learns to match true labels at  $t+n+k$ . The second term softly aligns the student’s long-horizon distribution with the teacher’s nearer-horizon distribution, effectively distilling “future” uncertainty 1(a).

In practice, we set  $\mathcal{L}_{\text{task}}$  to cross-entropy (for classification) or MSE (for regression). We pretrain  $T_\phi$  on its  $n$ -step task, then freeze it while training  $S_\theta$  under the combined FGL loss. Figure 1b illustrates the offset in the data flow.

In classic distillation [9], both teacher and student forecast the *same* horizon from identical inputs. FGL instead introduces a *temporal offset*: the teacher’s logits come from a shifted time step  $t+k$ , providing an extra supervisory signal drawn from the near future.

## Patient Specific Prediction Implementation

On the CHBMIT dataset, FGL was performed by first pre-training a unique teacher model for seizure detection on each patient for 50 epochs. During this pre-training phase, preictal segments were excluded, as their inclusion would reduce the uncertainty we aim to distill during the student training phase. Next, during the training of the student model over 25 epochs, each data point was fed into both the student and teacher models, and the corresponding class probabilities were obtained. The loss function defined in Equation 1 was then used to compute the student model’s loss. A range of  $\alpha$  values was tested to balance the contributions of the cross-entropy and KL divergence components of the loss function. The optimal  $\alpha$  for each patient was selected based on a hyperparameter sweep, with detailed results presented in Supplementary Figure 1. Different values of  $\alpha$  were tested to balance the cross-entropy and KL divergence components of the loss, with the optimal value selected through a hyperparameter sweep for each patient. The temperature parameter for the KD loss

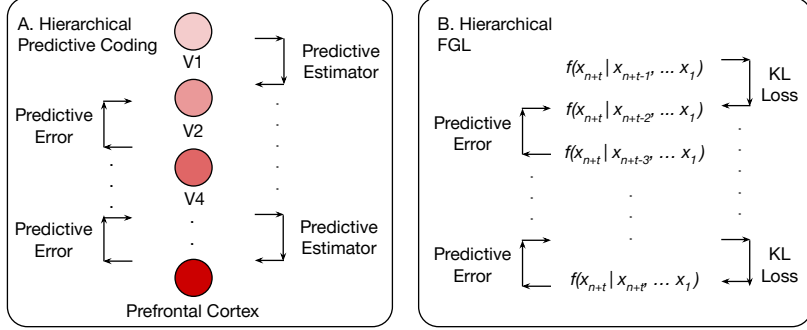


**Fig. 5: Predictive Coding and FGL** (A) Illustration of predictive coding in the brain. Information is received by the primary visual cortex (V1), which then propagates to different areas of the brain with more complex levels of abstraction. This propagation takes the form as a predictive estimator: higher level areas aid in prediction of lower level areas. The difference between the prediction and true output is the predictive error. Areas with lighter colors represent low-level abstractions, where darker colors represent the increasing representational demand (thoughts, movement, etc). (B) Hierarchical FGL propagates information via uncertainty, in other words, FGL substitutes the predictive estimator with the uncertainty of each layer. This uncertainty is conveyed via the KL divergence of between each layer’s probability distribution with the successive layer. The difference between each layer’s prediction and true output is the predictive error. In both models, areas lower in the hierarchy process information in a delayed manner, as they are the last to receive it. As the demand for complexity increases, so does the predictive error.

was fixed at  $T = 4$ . We used the SGD optimizer with a learning rate of  $5 \times 10^{-4}$ . Both the student and teacher models were implemented as CNN-LSTM architectures.

## Patient Non-Specific Prediction Implementation

When future data from the same distribution as the student model is unavailable, it is still possible to train a teacher model using future data from an out-of-distribution source. We test this approach on the AES dataset, which contains only preictal samples without any labeled seizures. Due to the lack of corresponding seizure data, we use a separate dataset: the UPenn and Mayo Clinic seizure dataset [27] to create the teacher model.

The AES dataset comprises recordings from 5 dogs and 2 humans, while the UPenn and Mayo Clinic dataset includes 4 dogs and 8 human patients. Given this discrepancy, we constructed two “universal teachers” from the latter dataset: one based on dog seizures and the other on human seizures. These universal teacher models were trained using a combined set of interictal data from selected patients, interspersed with randomly sampled seizures from a diverse pool of patients. This approach allows the teacher model to learn generalized seizure features from a wide variety of cases.

A challenge in using different data sources for the teacher model was the inconsistency in data characteristics and formats between datasets. We addressed this issue

by selecting the top  $k$  most significant EEG channels for each teacher model based on their contribution to seizure detection scores [28]. The number of selected channels was then adjusted based on the requirements of each student model, ensuring compatibility and effective knowledge transfer. As with the CHBMIT dataset, an ablation study of the influence of  $\alpha$  is provided in Supplementary Figure 1 and Supplementary Figure 2.

## Regression Forecasting Implementation

To quantify uncertainty in our regression forecasts, we map each continuous target value  $x_{t+n}$  onto a discrete probability distribution over  $B$  equally-spaced bins (Fig. 4a). Concretely, we first partition the full range of observed  $x$ -values into  $B$  contiguous intervals, then represent the "true" target by a one-hot vector indicating the bin that contains  $x_{t+n}$ . Our network's final layer has  $B$  neurons with softmax activations, so its output  $\mathbf{p} \in \Delta^{B-1}$  encodes a categorical distribution over these intervals. During distillation, the teacher supplies a softened  $\mathbf{p}^{(T)}$ , which the student matches via a KL-divergence loss; the hard one-hot label is still used in the cross-entropy term. Increasing  $B$  narrows each interval—leading to finer-grained value ranges and tighter uncertainty bounds—at the expense of making the classification task more difficult. This binning strategy thus lets us reduce a regression problem to a probability-distribution prediction, enabling us to leverage standard classification losses (cross-entropy + KL) while still recovering a real-valued forecast (e.g., by taking the expectation over bin centers).

In addition, we reformulate the tasks of the teacher and student models to better align with regression objectives. The teacher model performs next-step forecasting, while the student model focuses on longer-term predictions. This difference in forecasting horizons explicitly enforces a variance in timescales between the models. More specifically, given an input sample at  $x_t$ , the student model aims to predict  $n$  steps into the future, targeting  $x_{t+n}$ . In contrast, the teacher model is tasked with predicting the immediate next step and is provided with the input data at  $x_{t+n-1}$ .

Similar to event prediction, the teacher model is pretrained first, followed by inference within the student training loop, where the loss defined in Equation (1) is computed. During model testing, we select the neuron with the highest probability and compute the corresponding MSE, aligning this approach with traditional regression evaluation methods. Full experimental details can be found in Supplementary Note 2.

## Future Guided Learning And Predictive Coding

The teacher and student models can be described more precisely using a Bayesian prediction framework. The teacher, with access to  $n$  future points, has predictive density

$$p_T(x_{t+n}) = \int f(x_{t+n} | \theta) \pi(\theta | x_{1:t+n-1}) d\theta,$$

while the student, limited to the current window, uses

$$p_S(x_{t+n}) = \int f(x_{t+n} | \theta) \pi(\theta | x_{1:t}) d\theta.$$

Their divergence is

$$D_{\text{KL}}(p_T \| p_S) = \int p_T(x) \ln \frac{p_T(x)}{p_S(x)} dx,$$

quantifying how much “extra” information the teacher holds over the student as the horizon grows.

Rather than distilling directly from the longest-horizon teacher, we chain predictions through intermediate models at steps  $t+1, \dots, t+n-1$ . Each acts as both student (to its predecessor) and teacher (to its successor), propagating uncertainty down the hierarchy.

This approach bears similarity to a potential implementation of hierarchical predictive coding in the brain. Low-level cortical areas, such as the primary visual cortex (V1), function analogously to the intermediate models in hierarchical FGL, as they process detailed sensory inputs over short timescales (e.g.,  $f(x_{n+t}|x_{n+t-1}, \dots, x_t)$ ). In contrast, higher-level cortical areas like the prefrontal cortex correspond to the bottommost student model,  $f(x_{n+t}|x_n, \dots, x_t)$ , as they integrate abstract patterns and process temporally delayed information over longer timescales. A visual representation of this hierarchical structure is provided in Figure 5.

In practice, true posteriors are intractable. We therefore treat each  $p_T$  as a variational surrogate  $q(v)$  and each  $p_S$  as a prior  $p(v)$ , optimizing the usual ELBO:

$$\ln p(u) = -F + D_{\text{KL}}(q(v) \| p(v | u)),$$

where  $F$  is the free energy (a lower bound on surprise) [20, 29]. Finally, assuming Gaussian predictive distributions gives the familiar precision-weighted error form:

$$\ln p(u) \approx -\frac{1}{2} \left[ \ln \Sigma_S + \frac{(v_S - \Phi)^2}{\Sigma_S} + \ln \Sigma_T + \frac{(u - g(\Phi))^2}{\Sigma_T} \right].$$

Minimizing this drives the student toward the teacher’s richer, future-informed predictions.

## Data availability statement

All datasets used in this study are publicly available:

- **CHB–MIT Scalp EEG Database:** Available at <https://physionet.org/content/chbmit/1.0.0/>.
- **Kaggle Seizure Prediction Challenge:** Available at <https://www.kaggle.com/competitions/seizure-prediction>.
- **Kaggle UPenn & Mayo Clinic Seizure Detection Challenge:** Available at <https://www.kaggle.com/competitions/seizure-detection>.

- **Synthetic Mackey–Glass time series** generated for this work using the standard Mackey–Glass delay differential equation (see Supplementary Note 2). Parameter settings and generation scripts are provided in the accompanying code repository (see Code availability, below); preprocessed train/test splits used in our experiments are included there for reproducibility.

## Code availability

Our code is publicly available at the following github repository: <https://github.com/SkyeGunasekaran/FutureGuidedLearning>

## Acknowledgments

This work is supported by the US National Science Foundation ECCS:2332166 (J.E.).

## Author Contributions Statement

S.G. and J.E. conceived the project, designed the experiments and drafted the manuscript; S.G. performed all simulations; A.K., H.L. and R.Z. refined the experimental design; H.L. and L.P. derived the predictive-coding equations; O.K. supervised the analysis; J.E. oversaw the study. All authors reviewed the manuscript and approved the final version for submission.

## Competing Interests Statement

The authors declare no competing interests.

## References

- [1] Lai, G., Chang, W.-C., Yang, Y., Liu, H.: Modeling long-and short-term temporal patterns with deep neural networks. In: The 41st International ACM SIGIR Conference on Research & Development in Information Retrieval, pp. 95–104 (2018)
- [2] Ke, Y., Liang, Y., Shi, Z., Song, Z., Yang, C.: Curse of attention: A kernel-based perspective for why transformers fail to generalize on time series forecasting and beyond. arXiv preprint arXiv:2412.06061 (2024)
- [3] Das, A., Kong, W., Sen, R., Zhou, Y.: A decoder-only foundation model for time-series forecasting. arXiv preprint arXiv:2310.10688 (2023)
- [4] Bifet, A., Gavalda, R.: Learning from time-changing data with adaptive windowing. In: Proceedings of the 2007 SIAM International Conference on Data Mining, pp. 443–448 (2007). SIAM
- [5] Gama, J., Medas, P., Castillo, G., Rodrigues, P.: Learning with drift detection. In: Advances in Artificial Intelligence–SBIA 2004: 17th Brazilian Symposium on

Artificial Intelligence, Sao Luis, Maranhao, Brazil, September 29-Ocotber 1, 2004. Proceedings 17, pp. 286–295 (2004). Springer

- [6] Žliobaité, I.: Learning under concept drift: an overview. arXiv preprint arXiv:1010.4784 (2010)
- [7] Oprea, S., Martinez-Gonzalez, P., Garcia-Garcia, A., Castro-Vargas, J.A., Orts-Escolano, S., Garcia-Rodriguez, J., Argyros, A.: A review on deep learning techniques for video prediction. *IEEE Transactions on Pattern Analysis and Machine Intelligence* **44**(6), 2806–2826 (2020)
- [8] Baevski, A., Zhou, Y., Mohamed, A., Auli, M.: wav2vec 2.0: A framework for self-supervised learning of speech representations. *Advances in neural information processing systems* **33**, 12449–12460 (2020)
- [9] Hinton, G., Vinyals, O., Dean, J.: Distilling the knowledge in a neural network. arXiv preprint arXiv:1503.02531 (2015)
- [10] Chebotar, Y., Waters, A.: Distilling knowledge from ensembles of neural networks for speech recognition. In: *Interspeech*, pp. 3439–3443 (2016)
- [11] Choi, K., Kersner, M., Morton, J., Chang, B.: Temporal knowledge distillation for on-device audio classification. In: *ICASSP 2022-2022 IEEE International Conference on Acoustics, Speech and Signal Processing (ICASSP)*, pp. 486–490 (2022). IEEE
- [12] Zhang, Y., Liu, L., Liu, L.: Cuing without sharing: A federated cued speech recognition framework via mutual knowledge distillation. In: *Proceedings of the 31st ACM International Conference on Multimedia*, pp. 8781–8789 (2023)
- [13] Huang, M., You, Y., Chen, Z., Qian, Y., Yu, K.: Knowledge distillation for sequence model. In: *Interspeech*, pp. 3703–3707 (2018)
- [14] Von Helmholtz, H.: *Handbuch der Physiologischen Optik* vol. 9. Voss, ??? (1867)
- [15] Friston, K.: A theory of cortical responses. *Philosophical transactions of the Royal Society B: Biological sciences* **360**(1456), 815–836 (2005)
- [16] Spratling, M.W.: Predictive coding as a model of response properties in cortical area v1. *Journal of neuroscience* **30**(9), 3531–3543 (2010)
- [17] Keller, G.B., Mrsic-Flogel, T.D.: Predictive processing: a canonical cortical computation. *Neuron* **100**(2), 424–435 (2018)
- [18] Rao, R.P., Ballard, D.H.: Predictive coding in the visual cortex: a functional interpretation of some extra-classical receptive-field effects. *Nature neuroscience* **2**(1), 79–87 (1999)

- [19] Spratling, M.W.: A hierarchical predictive coding model of object recognition in natural images. *Cognitive computation* **9**(2), 151–167 (2017)
- [20] Millidge, B., Seth, A., Buckley, C.L.: Predictive coding: a theoretical and experimental review. *arXiv preprint arXiv:2107.12979* (2021)
- [21] Friston, K.: Does predictive coding have a future? *Nature neuroscience* **21**(8), 1019–1021 (2018)
- [22] Oord, A.v.d., Li, Y., Vinyals, O.: Representation learning with contrastive predictive coding. *arXiv preprint arXiv:1807.03748* (2018)
- [23] Lotter, W., Kreiman, G., Cox, D.: Deep predictive coding networks for video prediction and unsupervised learning. *arXiv preprint arXiv:1605.08104* (2016)
- [24] Hussein, R., Lee, S., Ward, R.: Multi-channel vision transformer for epileptic seizure prediction. *Biomedicines* **10**(7), 1551 (2022)
- [25] Shahbazi, M., Aghajan, H.: A generalizable model for seizure prediction based on deep learning using cnn-lstm architecture. In: 2018 IEEE Global Conference on Signal and Information Processing (GlobalSIP), pp. 469–473 (2018). IEEE
- [26] Yang, Y., Truong, N.D., Eshraghian, J.K., Nikpour, A., Kavehei, O.: Weak self-supervised learning for seizure forecasting: a feasibility study. *Royal Society Open Science* **9**(8), 220374 (2022)
- [27] Kaggle: UPenn and Mayo Clinic's Seizure Detection Challenge. <https://www.kaggle.com/c/seizure-detection> (2014)
- [28] Truong, N.D., Kuhlmann, L., Bonyadi, M.R., Yang, J., Faulks, A., Kavehei, O.: Supervised learning in automatic channel selection for epileptic seizure detection. *Expert Systems with Applications* **86**, 199–207 (2017)
- [29] Bogacz, R.: A tutorial on the free-energy framework for modelling perception and learning. *Journal of mathematical psychology* **76**, 198–211 (2017)
- [30] Beghi, E., Giussani, G., Nichols, E., Abd-Allah, F., Abdela, J., Abdelalim, A., Abraha, H.N., Adib, M.G., Agrawal, S., Alahdab, F., *et al.*: Global, regional, and national burden of epilepsy, 1990–2016: a systematic analysis for the global burden of disease study 2016. *The Lancet Neurology* **18**(4), 357–375 (2019)
- [31] Abbasi, B., Goldenholz, D.M.: Machine learning applications in epilepsy. *Epilepsia* **60**(10), 2037–2047 (2019)
- [32] Siddiqui, M.K., Morales-Menendez, R., Huang, X., Hussain, N.: A review of epileptic seizure detection using machine learning classifiers. *Brain informatics* **7**(1), 5 (2020)

- [33] Kuhlmann, L., Lehnertz, K., Richardson, M.P., Schelter, B., Zaveri, H.P.: Seizure prediction—ready for a new era. *Nature Reviews Neurology* **14**(10), 618–630 (2018)
- [34] Jasper, H.H.: Ten-twenty electrode system of the international federation. *Electroencephalogr Clin Neurophysiol* **10**, 371–375 (1958)
- [35] Truong, N.D., Nguyen, A.D., Kuhlmann, L., Bonyadi, M.R., Yang, J., Ippolito, S., Kavehei, O.: Convolutional neural networks for seizure prediction using intracranial and scalp electroencephalogram. *Neural Networks* **105**, 104–111 (2018)
- [36] Murphy, K.P.: Machine Learning: a Probabilistic Perspective. MIT press, ??? (2012)

## Additional Seizure Information

### Epilepsy Background Information

Epilepsy is a neurological condition which affects millions of people worldwide. It is characterized by a rapid firing in brain activity, often leading to spasms and involuntary muscle movements. Events of epilepsy are referred to as “ictal” events, whereas pre-seizure and non-seizure periods are referred to as “preictal” and “interictal”, respectively [30].

Due to the unpredictable nature of seizures, there has been a widespread effort for decades to create accurate seizure prediction mechanisms [31, 32]. However, attempts to do so have faced many challenges due to patient specificity, high noise of signals, and sparseness of seizure events. To further complicate the task, there has been contradicting evidence regarding the relationship between preictal and ictal events [33].

Patients with epilepsy who are undergoing medical treatment are typically monitored via scalp EEG, in which a varying number of nodes are placed on the patients head according to the 10-20 international standard [34]. Clinicians are tasked with monitoring these signals actively, and can sound an alarm when a seizure takes place to alert medical staff. Therefore, having an accurate seizure forecasting mechanism can help alleviate this burden on hospitals [33].

### Seizure Data Preprocessing

Our preprocessing pipeline of EEG data is as follows. Patient data is classified into three separate categories: interictal, preictal, and ictal. With respect to preictal data, we use a seizure occurrence period of 30 minutes, and a seizure prediction horizon of 5 minutes. Data up to 5 minutes prior to seizure onset is concealed from the student, and the 30 minutes prior to this is labeled as preictal data [35]. Due to this restriction, patients whose preictal data was not long enough were omitted from the dataset.

Each data sample undergoes a short-time-fourier transform (STFT) with a window size of 30 seconds. On both preictal and ictal data, we apply oversampling by taking a sliding window of STFTs. These overlapping samples are removed in the testing set. Our train-test-split was created by concatenating all of the interictal data, and evenly distributing them between ictal or preictal periods. The final 35% of seizures, as well as their corresponding interictal data, are used for testing. No shuffling is performed to preserve the temporal order of data.

## Experimental Details

**Dataset splits.** For each patient we gather *all* annotated EEG segments:

1. every inter-ictal (I) segment, and
2. every ictal *or* pre-ictal (S) segment.

We then build a **balanced, chronological stream**

$$I_1 S_1 I_2 S_2 \dots$$

by interleaving the two classes so that each seizure block  $S_j$  is immediately preceded by the amount of inter-ictal data required to keep the cumulative class counts equal.<sup>1</sup> This balanced stream is split *contiguously*: the first 65% forms the training set and the final 35% the held-out test set. No window, channel, or seizure appears in both splits.

### Models compared:

- **Baseline (CNN-LSTM).** batch-norm  $\rightarrow$  Conv3D( $1 \rightarrow 16, k = (T/2, 5, 5), s = (1, 2, 2)$ )  $\rightarrow$  max-pool  $\rightarrow$  batch-norm  $\rightarrow$  Conv3D( $16 \rightarrow 32, k = 3, s = 1$ )  $\rightarrow$  avg-pool( $3, 2$ )  $\rightarrow$  3-layer LSTM (512 hidden)  $\rightarrow$  FC 512 to FC 256 to 2.
- **FGL (ours).** Teacher: Seizure-detector (CNN-LSTM Backbone) Student: Seizure-predictor (CNN-LSTM Backbone) Trained with the Future-Guided loss (Eq.1);  $\alpha \in \{0, 0.1, \dots, 1\}$ .
- **MViT.** Multi-scale Vision Transformer per EEG channel: patch size (5, 10), embed dim 128, 4 heads, hidden dim 256, 4 encoder layers, dropout 0.1. Channel embeddings are concatenated and fed to a linear head ( $128 \times C \rightarrow 2$ ).

**Optimisation and over-fitting control:** All models are trained with Adam ( $\text{lr} = 5 \times 10^{-4}, \beta_1 = 0.9, \beta_2 = 0.999, \varepsilon = 10^{-8}$ ); batch size 32; maximum 25 epochs. To guard against overfitting, each experiment is repeated with multiple random initializations on the same dataset, and stability is assessed across runs.

**Evaluation:** For each patient we conduct three independent trials and report mean  $\pm$  std. of sensitivity, false-positive rate (FPR), and AUC-ROC on the test split. The decision threshold is chosen per patient via Youden's  $J$  statistic. Results appear in Table 1; best numbers per patient are shown in **bold**. **Hardware:** All models were trained using an NVIDIA RTX 4080 GPU.

---

<sup>1</sup>The first block is always inter-ictal because patients typically enter the hospital in a non-seizure state.

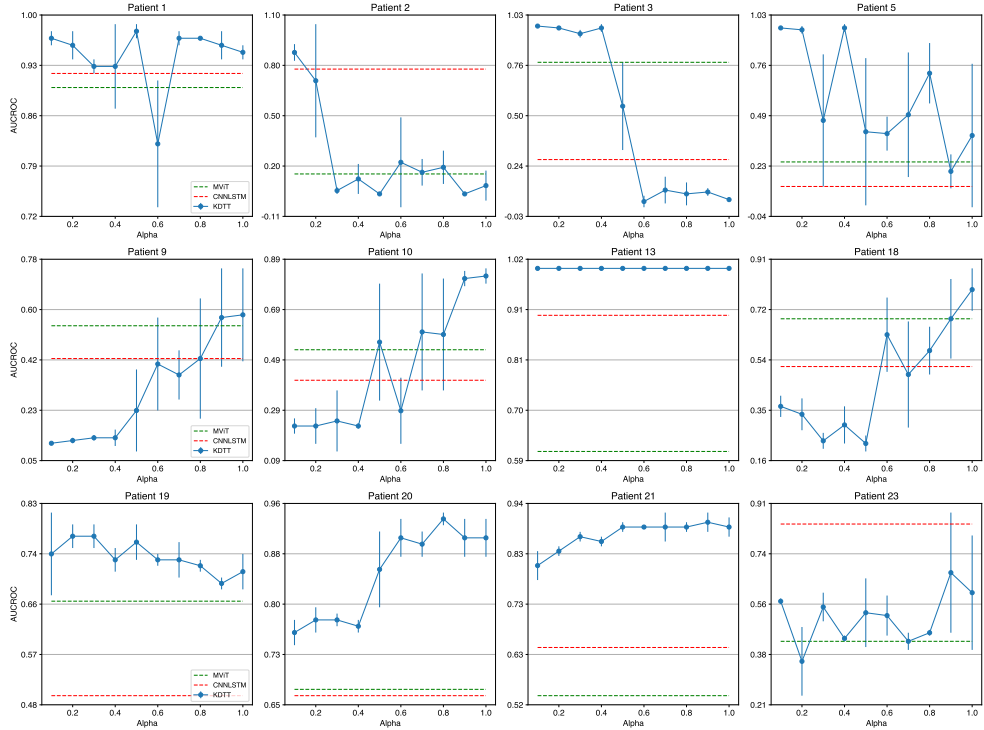


**Fig. 6: CHBMIT ablation study on alpha.** MViT results are represented as a dashed red line, and CNNLSTM results as a dashed green line.

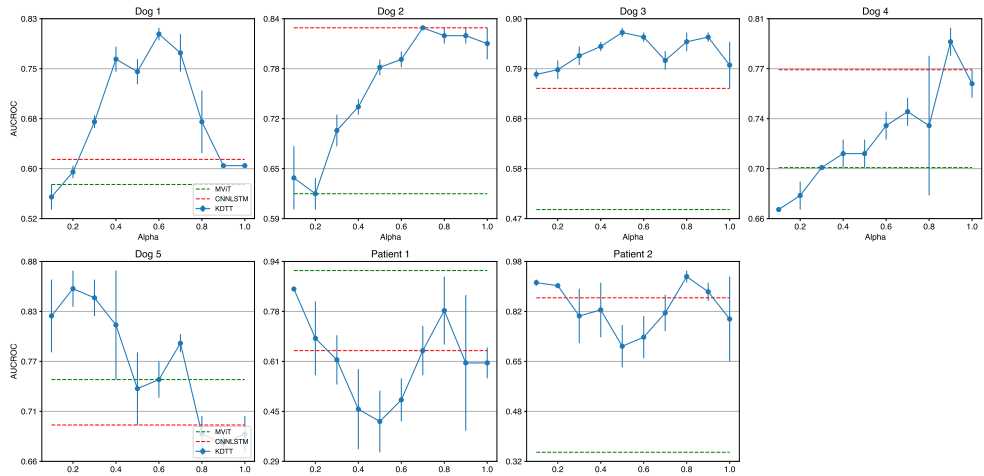


**Fig. 7: AES ablation study on alpha.** MViT results are represented as a dashed red line, and CNNLSTM results as a dashed green line.

**Table 1:** CHBMIT Comparison with SOTA

| Patient | MViT                   |                        |                        | CNNLSTM                |                        |                        | FGL                    |                        |                        |
|---------|------------------------|------------------------|------------------------|------------------------|------------------------|------------------------|------------------------|------------------------|------------------------|
|         | FPR                    | Sensitivity            | AUCROC                 | FPR                    | Sensitivity            | AUCROC                 | FPR                    | Sensitivity            | AUCROC                 |
| 1       | <b>0.02</b> $\pm$ 0.02 | 0.82 $\pm$ 0.22        | 0.90 $\pm$ 0.12        | 0.11 $\pm$ 0.12        | 0.88 $\pm$ 0.10        | 0.92 $\pm$ 0.97        | 0.04 $\pm$ 0.01        | <b>0.89</b> $\pm$ 0.04 | <b>0.98</b> $\pm$ 0.01 |
| 2       | 0.63 $\pm$ 0.45        | 0.66 $\pm$ 0.47        | 0.15 $\pm$ 0.19        | 0.35 $\pm$ 0.33        | <b>0.89</b> $\pm$ 0.15 | 0.78 $\pm$ 0.17        | <b>0.10</b> $\pm$ 0.04 | 0.83 $\pm$ 0.18        | <b>0.88</b> $\pm$ 0.05 |
| 3       | 0.16 $\pm$ 0.04        | 0.66 $\pm$ 0.23        | 0.78 $\pm$ 0.15        | 0.42 $\pm$ 0.40        | 0.49 $\pm$ 0.41        | 0.27 $\pm$ 0.19        | <b>0.01</b> $\pm$ 0.01 | <b>0.90</b> $\pm$ 0.02 | <b>0.97</b> $\pm$ 0.01 |
| 5       | 0.61 $\pm$ 0.43        | 0.66 $\pm$ 0.47        | 0.25 $\pm$ 0.10        | 0.65 $\pm$ 0.46        | 0.67 $\pm$ 0.47        | 0.12 $\pm$ 0.10        | <b>0.07</b> $\pm$ 0.00 | <b>0.97</b> $\pm$ 0.01 | <b>0.96</b> $\pm$ 0.01 |
| 9       | <b>0.20</b> $\pm$ 0.16 | 0.41 $\pm$ 0.41        | 0.54 $\pm$ 0.21        | 0.64 $\pm$ 0.45        | 0.67 $\pm$ 0.47        | 0.42 $\pm$ 0.10        | 0.60 $\pm$ 0.04        | <b>0.94</b> $\pm$ 0.02 | <b>0.57</b> $\pm$ 0.18 |
| 10      | <b>0.25</b> $\pm$ 0.17 | 0.48 $\pm$ 0.13        | 0.53 $\pm$ 0.17        | 0.56 $\pm$ 0.38        | 0.61 $\pm$ 0.34        | 0.41 $\pm$ 0.13        | 0.26 $\pm$ 0.04        | <b>0.65</b> $\pm$ 0.07 | <b>0.81</b> $\pm$ 0.03 |
| 13      | 0.18 $\pm$ 0.14        | 0.67 $\pm$ 0.36        | 0.61 $\pm$ 0.32        | 0.11 $\pm$ 0.10        | <b>0.99</b> $\pm$ 0.01 | 0.90 $\pm$ 0.10        | <b>0.00</b> $\pm$ 0.00 | <b>0.99</b> $\pm$ 0.01 | <b>1.00</b> $\pm$ 0.00 |
| 18      | <b>0.30</b> $\pm$ 0.10 | 0.68 $\pm$ 0.15        | <b>0.69</b> $\pm$ 0.07 | 0.54 $\pm$ 0.28        | 0.64 $\pm$ 0.26        | 0.51 $\pm$ 0.03        | 0.43 $\pm$ 0.14        | <b>0.88</b> $\pm$ 0.06 | <b>0.69</b> $\pm$ 0.15 |
| 19      | <b>0.07</b> $\pm$ 0.05 | 0.47 $\pm$ 0.33        | 0.66 $\pm$ 0.23        | 0.80 $\pm$ 0.04        | <b>0.97</b> $\pm$ 0.01 | 0.50 $\pm$ 0.07        | 0.48 $\pm$ 0.10        | 0.89 $\pm$ 0.07        | <b>0.76</b> $\pm$ 0.03 |
| 20      | 0.38 $\pm$ 0.07        | <b>0.98</b> $\pm$ 0.03 | 0.67 $\pm$ 0.09        | 0.45 $\pm$ 0.03        | 0.95 $\pm$ 0.06        | 0.66 $\pm$ 0.07        | <b>0.13</b> $\pm$ 0.03 | 0.86 $\pm$ 0.02        | <b>0.94</b> $\pm$ 0.01 |
| 21      | 0.60 $\pm$ 0.03        | <b>1.00</b> $\pm$ 0.00 | 0.54 $\pm$ 0.03        | 0.49 $\pm$ 0.14        | <b>0.97</b> $\pm$ 0.02 | 0.64 $\pm$ 0.18        | <b>0.12</b> $\pm$ 0.02 | 0.73 $\pm$ 0.04        | <b>0.90</b> $\pm$ 0.02 |
| 23      | 0.62 $\pm$ 0.06        | <b>1.00</b> $\pm$ 0.00 | 0.43 $\pm$ 0.02        | <b>0.20</b> $\pm$ 0.27 | 0.92 $\pm$ 0.12        | <b>0.84</b> $\pm$ 0.22 | 0.50 $\pm$ 0.08        | <b>1.00</b> $\pm$ 0.00 | 0.67 $\pm$ 0.21        |
| AVG     | 0.33 $\pm$ 0.21        | 0.70 $\pm$ 0.19        | 0.56 $\pm$ 0.20        | 0.44 $\pm$ 0.20        | 0.80 $\pm$ 0.16        | 0.58 $\pm$ 0.24        | <b>0.22</b> $\pm$ 0.01 | <b>0.87</b> $\pm$ 0.02 | <b>0.84</b> $\pm$ 0.15 |

**Table 2:** AES Comparison with SOTA

| Patient | MViT                   |                        |                        | CNNLSTM                |                        |                        | FGL                    |                        |                        |
|---------|------------------------|------------------------|------------------------|------------------------|------------------------|------------------------|------------------------|------------------------|------------------------|
|         | FPR                    | Sensitivity            | AUCROC                 | FPR                    | Sensitivity            | AUCROC                 | FPR                    | Sensitivity            | AUCROC                 |
| Dog 1   | 0.63 $\pm$ 0.06        | 0.93 $\pm$ 0.05        | 0.57 $\pm$ 0.00        | 0.62 $\pm$ 0.02        | <b>1.00</b> $\pm$ 0.00 | 0.61 $\pm$ 0.01        | <b>0.37</b> $\pm$ 0.05 | 0.99 $\pm$ 0.01        | <b>0.81</b> $\pm$ 0.01 |
| Dog 2   | <b>0.22</b> $\pm$ 0.07 | 0.48 $\pm$ 0.04        | 0.62 $\pm$ 0.01        | 0.34 $\pm$ 0.03        | <b>0.93</b> $\pm$ 0.03 | <b>0.83</b> $\pm$ 0.00 | 0.40 $\pm$ 0.02        | <b>0.93</b> $\pm$ 0.01 | <b>0.83</b> $\pm$ 0.00 |
| Dog 3   | 0.82 $\pm$ 0.16        | <b>0.87</b> $\pm$ 0.17 | 0.49 $\pm$ 0.02        | 0.35 $\pm$ 0.17        | 0.73 $\pm$ 0.05        | 0.75 $\pm$ 0.07        | <b>0.20</b> $\pm$ 0.08 | 0.71 $\pm$ 0.07        | <b>0.87</b> $\pm$ 0.01 |
| Dog 4   | 0.36 $\pm$ 0.08        | 0.66 $\pm$ 0.08        | 0.70 $\pm$ 0.02        | <b>0.35</b> $\pm$ 0.05 | 0.83 $\pm$ 0.05        | 0.77 $\pm$ 0.01        | <b>0.35</b> $\pm$ 0.02 | <b>0.87</b> $\pm$ 0.02 | <b>0.79</b> $\pm$ 0.01 |
| Dog 5   | 0.37 $\pm$ 0.04        | 0.93 $\pm$ 0.02        | 0.75 $\pm$ 0.02        | 0.47 $\pm$ 0.03        | <b>0.97</b> $\pm$ 0.01 | 0.70 $\pm$ 0.01        | <b>0.27</b> $\pm$ 0.07 | 0.88 $\pm$ 0.00        | <b>0.85</b> $\pm$ 0.02 |
| Human 1 | <b>0.20</b> $\pm$ 0.07 | 0.89 $\pm$ 0.03        | <b>0.91</b> $\pm$ 0.04 | 0.51 $\pm$ 0.16        | 0.91 $\pm$ 0.09        | 0.65 $\pm$ 0.17        | 0.28 $\pm$ 0.01        | <b>0.96</b> $\pm$ 0.02 | 0.85 $\pm$ 0.00        |
| Human 2 | 0.98 $\pm$ 0.00        | <b>1.00</b> $\pm$ 0.00 | 0.35 $\pm$ 0.01        | <b>0.21</b> $\pm$ 0.08 | 0.82 $\pm$ 0.10        | 0.86 $\pm$ 0.07        | 0.28 $\pm$ 0.13        | 0.90 $\pm$ 0.06        | <b>0.93</b> $\pm$ 0.02 |
| AVG     | 0.51 $\pm$ 0.28        | 0.82 $\pm$ 0.16        | 0.63 $\pm$ 0.15        | 0.40 $\pm$ 0.12        | 0.88 $\pm$ 0.08        | 0.78 $\pm$ 0.06        | <b>0.30</b> $\pm$ 0.02 | <b>0.89</b> $\pm$ 0.01 | <b>0.85</b> $\pm$ 0.01 |

# Mackey Glass Experiments

## Experimental Details

The Mackey-Glass (MG) equation is a delay differential equation used to model chaotic time-series data. It is defined as follows:

$$\frac{dP(t)}{dt} = \frac{\beta_0 \theta^n P(t - \tau)}{\theta^n + P(t - \tau)^n} - \gamma P(t) \quad (2)$$

where:

- $P(t)$ : The state variable at time  $t$ .
- $\tau$ : The time delay parameter.
- $\beta_0$ : The growth rate parameter.
- $\theta$ : The scaling parameter.
- $n$ : The exponent controlling the nonlinearity.
- $\gamma$ : The decay rate.

For our experiments, we used the following parameter values:

- $\tau = 17$
- Initial condition  $P(0) = 0.9$
- $n = 10$
- $\beta_0 = 0.2$
- $\gamma = 0.1$
- Time step size  $dt = 1.0$
- Lookback window = 8

**Dataset splits.** Given the parameters above, we generate a trajectory of length 10 000, use the first 6 000 points for training, the next 2 000 points for validation, and the final 2 000 for testing (60% / 20% / 20%).

**Models compared:**

- **Baseline (RNN).** RNN( $8 \rightarrow \text{bin\_size}, h = 128, l = 2$ )  $\rightarrow$  FC 128 to FC 128 to  $\text{bin\_size}$ .
- **FGL (ours).** Teacher: 1-step predictor (RNN Backbone) Student: N-step predictor (RNN Backbone) Trained with the Future-Guided loss (Eq. 1);  $\alpha \in \{0 \dots 1\}$ .

**Optimization and over-fitting control:** All models are trained with Adam ( $\text{lr} = 1 \times 10^{-4}$ ,  $\beta_1 = 0.9$ ,  $\beta_2 = 0.999$ ; batch size 128). We employ dropout (rate = 0.2) for regularization, fix the training budget to 50 epochs, and initialize random seeds at the start of each training regime. Early stopping (patience = 5 epochs, tolerance =  $1 \times 10^{-4}$ ) is applied by monitoring performance on the validation set each epoch, and the best checkpoint is restored before final evaluation. **Hardware:** All models were trained using an NVIDIA RTX 4080 GPU.

**Table 3:** FGL Results on Mackey–Glass

| Horizon    | Bins = 25 |                |                |          | Bins = 50      |                |  |  |
|------------|-----------|----------------|----------------|----------|----------------|----------------|--|--|
|            | Baseline  | $\alpha = 0.5$ | $\alpha = 0.0$ | Baseline | $\alpha = 0.5$ | $\alpha = 0.0$ |  |  |
| 2          | 1.55      | 1.44           | 1.44           | 5.07     | 4.55           | 5.20           |  |  |
| 3          | 2.65      | 2.27           | 2.27           | 9.38     | 8.05           | 7.96           |  |  |
| 4          | 3.60      | 3.12           | 3.16           | 12.61    | 10.67          | 10.77          |  |  |
| 5          | 4.94      | 4.29           | 4.30           | 17.64    | 14.42          | 13.86          |  |  |
| 6          | 6.34      | 5.37           | 6.86           | 20.61    | 17.51          | 17.42          |  |  |
| 7          | 5.83      | 7.45           | 5.60           | 23.61    | 18.37          | 19.01          |  |  |
| 8          | 6.37      | 5.80           | 5.63           | 30.71    | 17.34          | 18.59          |  |  |
| 9          | 6.18      | 5.14           | 5.00           | 20.79    | 16.49          | 14.45          |  |  |
| 10         | 5.21      | 3.70           | 3.98           | 16.94    | 11.56          | 12.75          |  |  |
| 11         | 3.78      | 2.83           | 3.18           | 14.60    | 9.00           | 9.73           |  |  |
| 12         | 3.04      | 2.39           | 2.66           | 11.48    | 8.67           | 9.58           |  |  |
| 13         | 2.82      | 2.14           | 2.36           | 195.62   | 9.39           | 9.90           |  |  |
| 14         | 2.61      | 2.02           | 2.30           | 9.53     | 9.06           | 8.73           |  |  |
| 15         | 2.30      | 1.91           | 2.25           | 8.22     | 8.44           | 9.35           |  |  |
| <b>Avg</b> | 4.09      | <b>3.56</b>    | 3.64           | 28.34    | <b>11.68</b>   | 11.95          |  |  |

## Mackey Glass Dataset Results

### Page Hinkley Drift Adaptation Experiment

In this supplementary experiment, we evaluate whether post-hoc drift adaptation—specifically a Page–Hinkley-can compensate for FGL. To do so, we take our three Mackey–Glass forecasting models (the baseline, the FGL student with  $\alpha = 0.0$ , and the FGL student with  $\alpha = 0.5$ ), and expose each to identical PH retraining. By showing that the relative performance ranking established by FGL during training persists even after this adaptive correction, we demonstrate that the advantages of future-guided learning are not supplanted by simple post-hoc methods, but rather remain an independent—and complementary—means of improving forecast accuracy.

Let  $e_t$  be the instantaneous forecast error (MSE) at time  $t$ , and let

$$\bar{e}_t = \frac{1}{t} \sum_{i=1}^t e_i$$

be its cumulative running mean. The PH test tracks the one-sided cumulative deviation

$$u_t = e_t - \bar{e}_{t-1} - \delta, \quad S_t = \sum_{i=1}^t u_i, \quad S_{\min}(t) = \min_{1 \leq i \leq t} S_i.$$

A drift alarm is raised whenever

$$S_t - S_{\min}(t) > \lambda,$$

where  $\delta > 0$  is a small tolerance (to avoid false alarms) and  $\lambda > 0$  is the detection threshold. In our setup we use a sliding window of length 3 to recompute  $\bar{e}$  and reset

$S_t$  after each retraining, and we choose  $(\delta, \lambda)$  per bin-count. Upon alarm, we retrain each model for 3 epochs on the most recent data to correct for drift.

**Table 4:** FGL Results on Mackey–Glass w/ Page Hinkley

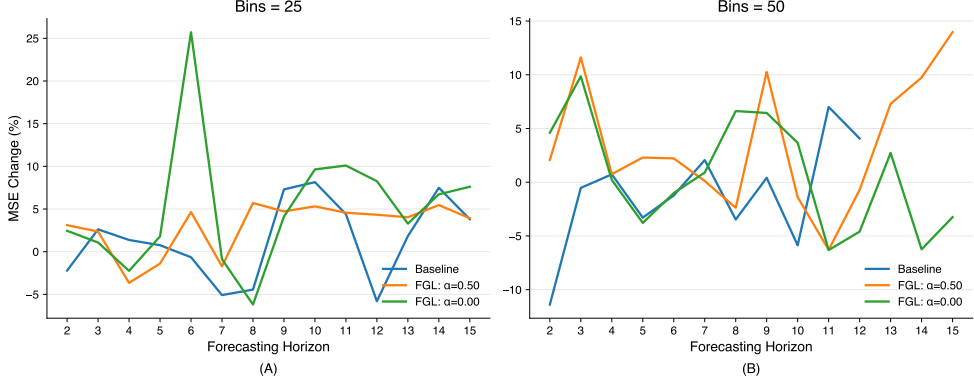
| Horizon    | Bins = 25 |                |                | Bins = 50 |                |                |
|------------|-----------|----------------|----------------|-----------|----------------|----------------|
|            | Baseline  | $\alpha = 0.5$ | $\alpha = 0.0$ | Baseline  | $\alpha = 0.5$ | $\alpha = 0.0$ |
| 2          | 1.59      | 1.40           | 1.41           | 5.65      | 4.45           | 4.96           |
| 3          | 2.58      | 2.22           | 2.25           | 9.43      | 7.12           | 7.18           |
| 4          | 3.55      | 3.23           | 3.23           | 12.52     | 10.59          | 10.74          |
| 5          | 4.90      | 4.35           | 4.23           | 18.22     | 14.09          | 14.38          |
| 6          | 6.38      | 5.12           | 5.09           | 20.86     | 17.12          | 17.59          |
| 7          | 6.13      | 7.58           | 5.65           | 23.13     | 18.35          | 18.84          |
| 8          | 6.65      | 5.47           | 5.98           | 31.78     | 17.75          | 17.36          |
| 9          | 5.72      | 4.90           | 4.80           | 20.71     | 14.79          | 13.52          |
| 10         | 4.79      | 3.50           | 3.59           | 17.94     | 11.72          | 12.28          |
| 11         | 3.61      | 2.70           | 2.86           | 13.58     | 9.57           | 10.35          |
| 12         | 3.22      | 2.29           | 2.44           | 11.01     | 8.73           | 10.02          |
| 13         | 2.77      | 2.06           | 2.28           | 223.29    | 8.71           | 9.63           |
| 14         | 2.41      | 1.91           | 2.15           | 203.58    | 8.18           | 9.27           |
| 15         | 2.22      | 1.84           | 2.07           | 195.71    | 7.26           | 9.66           |
| <b>Avg</b> | 4.04      | 3.47           | <b>3.43</b>    | 57.67     | <b>11.32</b>   | 11.84          |

Table 1 demonstrates that, even after excluding non-convergent horizons, FGL with  $\alpha = 0.5$  and  $\alpha = 0.0$  both deliver substantial reductions in average MSE relative to the baseline. For Bins = 25, FGL reduces MSE by 14.1% ( $\alpha = 0.5$ ) & 15.1% ( $\alpha = 0.0$ ) when PH is enabled, and by 13.0% and 11.0% without PH. For Bins = 50, the corresponding improvements are 27.3% & 25.8% (with PH) and 23.4% & 21.8% (without PH). These results confirm that FGL’s advantage holds consistently across both  $\alpha$  settings and that applying PH on top of FGL yields an additional 2–3% MSE reduction, underscoring their complementary nature.

## Future Guided Learning and Predictive Coding

To connect FGL to predictive coding, we review the mathematical intuition behind this theory, as explored in prior work [20, 29]. Using the common mathematical formalisms from these publications, we summarize the relevant concepts in this Appendix to establish a link between predictive processing and FGL. Predictive coding networks can be defined as ensembles of units that compute the posterior probabilities of environmental states  $p(v|u)$  based on a top-down prior  $p(v)$  and a bottom-up likelihood  $p(u|v)$ . Assuming Gaussian distributions for these terms, Bayes’ theorem allows this computation to be expressed as:

$$p(v|u) = \frac{p(v)p(u|v)}{p(u)} = \frac{\frac{1}{\sqrt{2\pi\Sigma_p}} \exp\left(-\frac{(v-v_p)^2}{2\Sigma_p}\right) \frac{1}{\sqrt{2\pi\Sigma_u}} \exp\left(-\frac{(u-g(v))^2}{2\Sigma_u}\right)}{\int p(v)p(u|v), dv}. \quad (3)$$



**Fig. 8: Application of Page–Hinkley (PH) drift adaptation to FGL.** We applied the same online PH detector (3-sample sliding window, 3-epoch retraining) to three Mackey–Glass forecasters: Baseline (no FGL), FGL ( $\alpha = 0$ ), and FGL ( $\alpha = 0.5$ ). PH sensitivity parameters were tuned per bin count (25 bins:  $\delta = 0.130$ ,  $\lambda = 0.647$ ; 50 bins:  $\delta = 5.78$ ,  $\lambda = 7.84$ ), while all other hyperparameters match the original experiments. Each panel shows the per-horizon percentage change in MSE after retraining relative to the original forecasts. Both FGL students ( $\alpha = 0.0$  and  $\alpha = 0.5$ ) show a meaningful average reduction in MSE loss, whereas the baseline’s error actually increases. This demonstrates that training-time future guidance provides benefits that complement—not replace—post-hoc drift adaptation.

Here,  $v$  represents a scalar value of the environment, characterized by  $v_p$  and  $\Sigma_p$ , the mean and variance of its Gaussian distribution, respectively. Similarly,  $p(u|v)$  represents the likelihood, where the scalar  $u$  is modeled as the output of an activation function  $g(v)$  (e.g., the reflection of light from a surface) with variance  $\Sigma_u$ .

The denominator in Equation 3 serves as a normalization term that is computationally intractable for biological neural networks due to the need to integrate over all possible combinations of  $p(v)$  and  $p(u|v)$ . One possible simplification is maximum likelihood estimation (MLE), which identifies the value of  $v$  that maximizes  $p(v|u)$ . This value, denoted as  $\Phi$ , effectively replaces  $p(v)$  in an MLE framework. Since the denominator is absent from the left-hand side of Equation 3 under MLE, we can instead focus on the numerator and express its logarithm,  $F$ , as:

$$F = \ln(p(\Phi)p(u|\Phi)) = \ln p(\Phi) + \ln p(u|\Phi). \quad (4)$$

We thus derive:

$$\begin{aligned}
F &= \ln p(\Phi) + \ln p(u|\Phi) \\
&= \ln \left( \frac{1}{\sqrt{2\pi\Sigma_p}} \exp -\frac{(\Phi - v_p)^2}{2\Sigma_p} \right) + \ln \left( \frac{1}{\sqrt{2\pi\Sigma_u}} \exp -\frac{(u - g(\Phi))^2}{2\Sigma_u} \right) \\
&= \ln \left( \frac{1}{\sqrt{2\pi\Sigma_p}} \right) + \ln \left( \exp -\frac{(\Phi - v_p)^2}{2\Sigma_p} \right) + \ln \left( \frac{1}{\sqrt{2\pi\Sigma_u}} \right) + \ln \left( \exp -\frac{(u - g(\Phi))^2}{2\Sigma_u} \right) \\
&= \ln \left( \frac{1}{\sqrt{2\pi}} \right) - \frac{1}{2} \ln \Sigma_p - \frac{(\Phi - v_p)^2}{2\Sigma_p} + \ln \left( \frac{1}{\sqrt{2\pi}} \right) - \frac{1}{2} \ln \Sigma_u - \frac{(u - g(\Phi))^2}{2\Sigma_u} \\
&= \frac{1}{2} \left( -\ln \Sigma_p - \frac{(\Phi - v_p)^2}{\Sigma_p} - \ln \Sigma_u - \frac{(u - g(\Phi))^2}{\Sigma_u} \right) + C
\end{aligned} \tag{5}$$

Where  $C$  is a constant combining terms that do not depend on  $\Phi$ .

To determine the maximum likelihood estimate, we compute the derivative of  $F$  with respect to the surrogate value  $\Phi$ :

$$\begin{aligned}
\frac{\delta F}{\delta \Phi} &= \frac{1}{2} \left( \frac{\delta}{\delta \Phi} \left( -\frac{(u - g(\Phi))^2}{\Sigma_u} \right) + \frac{\delta}{\delta \Phi} \left( -\frac{(\Phi - v_p)^2}{\Sigma_p} \right) + \frac{\delta}{\delta \Phi} (-\ln \Sigma_u) + \frac{\delta}{\delta \Phi} (-\ln \Sigma_p) + \frac{\delta}{\delta \Phi} C \right) \\
&= \frac{1}{2} \left( \left( -\frac{1}{\Sigma_u} \frac{\delta}{\delta \Phi} (u - g(\Phi))^2 \right) + \left( -\frac{1}{\Sigma_p} \frac{\delta}{\delta \Phi} (\Phi - v_p)^2 \right) \right)
\end{aligned} \tag{6}$$

Applying the power rule  $(f(x)^n)' = nf(x)^{n-1}f'(x)$ :

$$\begin{aligned}
\frac{\delta F}{\delta \Phi} &= \frac{1}{2} \left( \left( -\frac{1}{\Sigma_u} 2(u - g(\Phi)) \frac{\delta}{\delta \Phi} (u - g(\Phi)) \right) + \left( -\frac{1}{\Sigma_p} 2(\Phi - v_p) \frac{\delta}{\delta \Phi} (\Phi - v_p) \right) \right) \\
&= \frac{1}{2} \left( \left( -\frac{1}{\Sigma_u} 2(u - g(\Phi)) \left( \frac{\delta}{\delta \Phi} u - \frac{\delta}{\delta \Phi} g(\Phi) \right) \right) + \left( -\frac{1}{\Sigma_p} 2(\Phi - v_p) \left( \frac{\delta}{\delta \Phi} \Phi - \frac{\delta}{\delta \Phi} v_p \right) \right) \right) \\
&= \frac{1}{2} \left( \left( -\frac{1}{\Sigma_u} 2(u - g(\Phi))(-g'(\Phi)) \right) + \left( -\frac{1}{\Sigma_p} 2(\Phi - v_p) \right) \right) \\
&= \left( \frac{1}{\Sigma_u} (u - g(\Phi))(g'(\Phi)) \right) + \left( -\frac{1}{\Sigma_p} (\Phi - v_p) \right) \\
&= \frac{(u - g(\Phi))}{\Sigma_u} g'(\Phi) + \frac{(v_p - \Phi)}{\Sigma_p}
\end{aligned} \tag{7}$$

For simplicity, we rewrite the terms as:

$$\begin{aligned}
\epsilon_p &= \frac{(v_p - \Phi)}{\Sigma_p} \\
\epsilon_u &= \frac{(u - g(\Phi))}{\Sigma_u},
\end{aligned} \tag{8}$$

where  $\epsilon_p$  represents the prediction error on the causes, and  $\epsilon_u$  represents the prediction error on the states [15]. Using these terms, the derivative of  $F$  with respect to  $\Phi$  becomes:

$$\frac{\delta F}{\delta \Phi} = \epsilon_u g'(\Phi) + \epsilon_p \quad (9)$$

This gradient can be reformulated as a learning rule:

$$\dot{\Phi} = \epsilon_u g'(\Phi) - \epsilon_p \quad (10)$$

Conceptually,  $\epsilon_p$  quantifies the prediction error on the causes, capturing the difference between the inferred value ( $\Phi$ ) and the model's prior expectation ( $v_p$ ) [20]. In contrast,  $\epsilon_u$  measures the prediction error on the states, reflecting the discrepancy between the observed value ( $u$ ) and the predicted value ( $g(\Phi)$ ). Simply put,  $\epsilon_p$  corresponds to errors at higher-level representations, while  $\epsilon_u$  pertains to raw differences between inferred and actual sensory inputs.

The function  $F$ , referred to as the variational free energy, serves as a key metric in predictive coding frameworks. While a detailed discussion is beyond the scope of this appendix,  $F$  intuitively relates to information-theoretic concepts, particularly as a lower bound on the model's surprise or uncertainty [15].

In predictive coding, one of the goals of a model is to maximize prediction efficiency and thus minimize both sources of prediction errors. At their minimal values, these errors converge to stable points,  $\epsilon_p$  and  $\epsilon_u$ , defined as:

$$\begin{aligned} \epsilon_p &= \frac{\Phi - v_p}{\Sigma_p} \\ \Sigma_p \epsilon_p &= \Phi - v_p \end{aligned} \quad (11)$$

$$\begin{aligned} \Phi - v_p - \Sigma_p \epsilon_p &= 0 \\ \epsilon_u &= \frac{u - g(\Phi)}{\Sigma_u} \\ \Sigma_u \epsilon_u &= u - g(\Phi) \end{aligned} \quad (12)$$

$$u - g(\Phi) - \Sigma_u \epsilon_u = 0$$

The dynamics of a system aiming to minimize prediction errors and infer the most likely value of  $\Phi$  under a MLE approach can then be described as:

$$\begin{aligned} \dot{\epsilon}_p &= \Phi - v_p - \Sigma_p \epsilon_p \\ \dot{\epsilon}_u &= u - g(\Phi) - \Sigma_u \epsilon_u \end{aligned} \quad (13)$$

This establishes an intuitive relationship between predictive coding and FGL. In predictive coding, the uncertainties  $\Sigma_p$  and  $\Sigma_u$  parameterize the model. Under an MLE approach, these parameters converge to the most likely value of the inputs, effectively discarding distributional information and reducing the computation to point estimates. While this simplification is efficient, it is inherently incompatible with FGL as presented, where the preservation of distributional richness is critical to leveraging temporal variance and uncertainty effectively.

An alternative to the MLE approach is the use of a “surrogate” distribution via variational inference [36]. Variational inference bypasses the computational intractability of normalization terms (Equation 3) and complex input distributions by introducing a new distribution  $q(v)$ , which has a standard form characterized by its mean and variance.

In the context of FGL, the student and teacher networks can be more accurately defined within a Bayesian framework. Here, the teacher model acts as a well-posed surrogate  $T \approx q(v)$ , while the student model is treated as a prior,  $S = p(v)$ . This framing allows the teacher model to serve as a surrogate representation to guide the student model, effectively approximating the posterior  $p(v|u)$  with  $q(v)$ .

The shift from MLE to variational inference involves minimizing the divergence between the surrogate distribution  $q(v)$  and the true posterior  $p(v|u)$ . This divergence is quantified using the Kullback-Leibler (KL) divergence:

$$KL(q(v), p(v|u)) = \int q(v) \ln \frac{q(v)}{p(v|u)} dv \quad (14)$$

While the KL divergence provides a useful metric, it is implausible for a biological network to directly measure this difference due to the same issue of computational intractability of  $p(v|u)$  that led to the use of MLE:

$$p(v|u) = \frac{p(u, v)}{p(u)} = \frac{p(u, v)}{\int p(v)p(u|v)dv} \quad (15)$$

Expanding the KL divergence using the above expression, we have:

$$\begin{aligned} KL(q(v), p(v|u)) &= \int q(v) \ln \frac{q(v)}{p(v|u)} dv \\ &= \int q(v) \ln \frac{q(v)p(u)}{p(u, v)} dv \\ &= \int q(v) \ln \frac{q(v)}{p(u, v)} dv + \int q(v) \ln p(u) dv \end{aligned} \quad (16)$$

Since the surrogate  $q(v)$  is a valid probability distribution that integrates to 1, the second term simplifies to  $\ln p(u)$ , yielding:

$$KL(q(v), p(v|u)) = \int q(v) \ln \frac{q(v)}{p(u, v)} dv + \ln p(u) \quad (17)$$

We define the first term as the variational free energy  $F$ , which avoids the need for computing the normalization term and as such, the student’s prior distribution becomes computationally tractable:

$$\begin{aligned} F &= \int q(v) \ln \frac{q(v)}{p(u, v)} dv \\ KL(q(v), p(v|u)) &= F + \ln p(u) \end{aligned} \quad (18)$$

since  $F$  depends on the surrogate distribution  $q(v)$ , the parameters which minimize the distance between the surrogate  $q(v)$  and the teacher’s posterior  $p(v|u)$ , are

identical to those which maximize  $F$ , which in turn negates the computation of the normalization term. Substituting  $F$ , we obtain:

$$\ln p(u) = -F + KL(q(v), p(v|u)) \quad (19)$$

The term  $\ln p(u)$ , derived above, represents the “surprise” associated with the student’s estimate  $p(u)$  of the actual value  $v$ , and is directly linked to the uncertainty of the student model. Since the KL divergence is strictly non-negative,  $F$  acts as a lower bound for the surprise  $\ln p(u)$ . Consequently, maximizing  $F$  corresponds to minimizing surprise or uncertainty of the student  $\ln p(u)$ , improving the surrogate approximation  $q(v)$ , and by extension, optimizing the student model with respect to the teacher in the context of FGL.

This concept of surprise is particularly valuable for updating uncertainty parameters within a network performing predictive computations, where  $\ln p(u)$  can be written as:

$$\begin{aligned} \ln p(u) &= F + KL(q(v), p(v|u)) \\ &= \frac{1}{2} \left[ -\ln \Sigma_p - \frac{(\Phi - v_p)^2}{\Sigma_p} - \ln \Sigma_u - \frac{(u - g(\Phi))^2}{\Sigma_u} \right] + C + KL(q(v), p(v|u)) \end{aligned} \quad (20)$$

Since the KL divergence is strictly non-negative, it can be absorbed into the constant  $C$  for simplicity, ensuring the expression focuses on terms directly impacting the uncertainty parameters.

Starting from this definition, we can now derive  $F$  to optimize  $v_p$ :

$$\begin{aligned} \frac{\delta F}{\delta v_p} &= \frac{1}{2} \left( \frac{\delta}{\delta v_p} \left( -\frac{(\Phi - v_p)^2}{\Sigma_p} \right) + \frac{\delta}{\delta v_p} \left( -\frac{(u - g(\Phi))^2}{\Sigma_u} \right) \right. \\ &\quad \left. + \frac{\delta}{\delta v_p} (-\ln \Sigma_u) + \frac{\delta}{\delta v_p} (-\ln \Sigma_p) \right) + \frac{\delta C}{\delta v_p} \\ &= \frac{1}{2} \frac{\delta}{\delta v_p} \left( -\frac{(\Phi - v_p)^2}{\Sigma_p} \right) \\ &= \frac{1}{2} \left( -\frac{1}{\Sigma_p} \right) \frac{\delta}{\delta v_p} (\Phi - v_p)^2 \\ &= -\frac{1}{\Sigma_p} (\Phi - v_p) \frac{\delta}{\delta v_p} (\Phi - v_p) \\ &= -\frac{1}{\Sigma_p} (\Phi - v_p) (0 - 1) \\ &= \frac{\Phi - v_p}{\Sigma_p}. \end{aligned} \quad (21)$$

The same can be done for  $\Sigma_p$ :

$$\begin{aligned}
\frac{\delta F}{\delta \Sigma_p} &= \frac{1}{2} \left( \frac{\delta}{\delta \Sigma_p} \left( -\frac{(\Phi - v_p)^2}{\Sigma_p} \right) + \frac{\delta}{\delta \Sigma_p} \left( -\frac{(u - g(\Phi))^2}{\Sigma_u} \right) \right. \\
&\quad \left. + \frac{\delta}{\delta \Sigma_p} (-\ln \Sigma_u) + \frac{\delta}{\delta \Sigma_p} (-\ln \Sigma_p) \right) + \frac{\delta C}{\delta \Sigma_p} \\
&= \frac{1}{2} \left( -\frac{\delta}{\delta \Sigma_p} \ln \Sigma_p + \left( -(\Phi - v_p)^2 \frac{\delta}{\delta \Sigma_p} (\Sigma_p^{-1}) \right) \right) \\
&= \frac{1}{2} \left( -\frac{1}{\Sigma_p} + (\Phi - v_p)^2 \frac{\delta \Sigma_p}{\Sigma_p^2} \right) \\
&= \frac{1}{2} \left( (\Phi - v_p)^2 \frac{\delta \Sigma_p}{\Sigma_p^2} - \frac{1}{\Sigma_p} \right) \\
&= \frac{1}{2} \left( \frac{(\Phi - v_p)^2}{\Sigma_p^2} - \frac{1}{\Sigma_p} \right).
\end{aligned} \tag{22}$$

Likewise, for  $\Sigma_u$ :

$$\begin{aligned}
\frac{\delta F}{\delta \Sigma_u} &= \frac{1}{2} \left( \frac{\delta}{\delta \Sigma_u} \left( -\frac{(\Phi - v_p)^2}{\Sigma_p} \right) + \frac{\delta}{\delta \Sigma_u} \left( -\frac{(u - g(\Phi))^2}{\Sigma_u} \right) \right. \\
&\quad \left. + \frac{\delta}{\delta \Sigma_u} (-\ln \Sigma_u) + \frac{\delta}{\delta \Sigma_u} (-\ln \Sigma_p) \right) + \frac{\delta C}{\delta \Sigma_u} \\
&= \frac{1}{2} \left( \frac{\delta}{\delta \Sigma_u} \left( -\frac{(u - g(\Phi))^2}{\Sigma_u} \right) - \frac{\delta}{\delta \Sigma_u} \ln \Sigma_u \right) \\
&= \frac{1}{2} \left( -(u - g(\Phi))^2 \frac{\delta}{\delta \Sigma_u} (\Sigma_u^{-1}) - \frac{1}{\Sigma_u} \right) \\
&= \frac{1}{2} \left( \frac{(u - g(\Phi))^2}{\Sigma_u^2} - \frac{1}{\Sigma_u} \right).
\end{aligned} \tag{23}$$

Yielding the learned parameters of a predictive coding network that performs equivalent computation to FGL as:

$$\begin{aligned}
\frac{\delta F}{\delta v_p} &= \frac{\Phi - v_p}{\Sigma_p} = \epsilon_p \\
\frac{\delta F}{\delta \Sigma_p} &= \frac{1}{2} \left( \frac{(\Phi - v_p)^2}{\Sigma_p^2} - \frac{1}{\Sigma_p} \right) = \frac{1}{2} (\epsilon_p^2 - \Sigma_p^{-1}) \\
\frac{\delta F}{\delta \Sigma_u} &= \frac{1}{2} \left( \frac{(u - g(\Phi))^2}{\Sigma_u^2} - \frac{1}{\Sigma_u} \right) = \frac{1}{2} (\epsilon_u^2 - \Sigma_u^{-1})
\end{aligned} \tag{24}$$

While these equations follow scalar notations, Bogacz [29] showed that they can trivially be extended to vector and matrices forms with neurobiologically plausible implementations that are computationally similar to FGL.

## Dataset I/O Summary

| Task          | Input $x_t$                    | Target $y_{t+\ell}$                |
|---------------|--------------------------------|------------------------------------|
| Seizure pred. | $N$ -ch EEG segment ( $F$ Hz)  | 3-way class (ictal / inter / pre)  |
| Mackey–Glass  | 1-D chaotic window ( $L = 8$ ) | Scalar at $t + \ell$ (discretised) |